Propagation of a strong x-ray pulse: Pulse compression, stimulated Raman scattering, amplified spontaneous emission, lasing without inversion, and four-wave mixing

Yu-Ping Sun,[1,2] Ji-Cai Liu,[2,*] Chuan-Kui Wang,[1,2] and Faris Gel'mukhanov[2]
[1] *College of Physics and Electronics, Shandong Normal University, 250014 Jinan, People's Republic of China*
[2] *Department of Theoretical Chemistry, School of Biotechnology, Royal Institute of Technology, S-10691 Stockholm, Sweden*

(Received 29 July 2009; published 20 January 2010)

We study the compression of strong x-ray pulses from x-ray free-electron lasers (XFELs) propagating through the resonant medium of atomic argon. The simulations are based on the three-level model with the frequency of the incident x-ray pulse tuned in the $2p_{3/2}$-$4s$ resonance. The pulse propagation is accompanied by the self-seeded stimulated resonant Raman scattering (SRRS). The SRRS starts from two channels of amplified spontaneous emission (ASE), $4s$-$2p_{3/2}$ and $3s$-$2p_{3/2}$, which form the extensive ringing pattern and widen the power spectrum. The produced seed field triggers the Stokes ASE channel $3s$-$2p_{3/2}$. The population inversion is quenched for longer propagation distances where the ASE is followed by the lasing without inversion (LWI), which amplifies the Stokes component. Both ASE and LWI reshape the input pulse: The compressed front part of the pulse (up to 100 as) is followed by the long tail of the ringing and beating between the pump and Stokes frequencies. The pump pulse also generates weaker Stokes and anti-Stokes fields caused by four-wave mixing. These four spectral bands have fine structures caused by the dynamical Stark effect. A slowdown of the XFEL pulse up to 78% of the speed of light in vacuum is found because of a large nonlinear refractive index.

DOI: 10.1103/PhysRevA.81.013812 PACS number(s): 42.65.Re, 32.80.Aa, 41.60.Cr

I. INTRODUCTION

X-ray free-electron lasers (XFELs) offer the unique opportunity of investigating phenomena related to the propagation of short and intense x-ray pulses [1–3]. The XFELs are expected to provide intensities about 10^{18}–10^{19} W/cm^2 and pulse durations $\lesssim 10$ fs using, for example, the slicing technique [1–4] or an energy-chirped electron beam [5]. Some of the strong x-ray field effects were recently [6,7] reported, where special attention was paid to the multicolor x-ray pump-probe spectroscopy [8–10]. We study the role of the strong and resonant x-ray pulse propagation in its shape and spectrum.

In this article we present a theoretical study of the propagation of strong x-ray pulses through the resonant medium of atomic argon. The carrier frequency of the input pulse is tuned in resonance with the $2p_{3/2}$-$4s$ transition. When the pulse area is larger than $\pi/2$, the pulse propagation is accompanied by two channels of amplified spontaneous emission (ASE), $4s$-$2p_{3/2}$ and $3s$-$2p_{3/2}$, with frequencies of 244.3 and 219.28 eV, respectively. The main goal of our study is the reshaping of the pulse during propagation with special attention to the compression of the pulse and its spectrum. The experiment scheme suggested here makes it possible to generate sub-fs x-ray pulses. The naive picture says that the Stokes ASE channel $3s$-$2p_{3/2}$ is not important because the resonant frequency of this channel differs greatly (about 25 eV) from the carrier frequency of the incident pulse. However, the simulations show a complete breakdown of the two-level approximation which ignores the $3s$-$2p_{3/2}$ channel. We study in detail the π, 2.5π, 3π, and 3.5π pulses which create the inversion of the population for both channels. The reshaping of the input pulse leads to an extensive tail in the power spectrum. Compared with spontaneous noise [1,4] or injection seeding, such a self-seeding offers considerable advantages because of the fast development of the stimulated resonant Raman scattering (SRRS) and simplicity. The produced seed field triggers the Stokes ASE channel. Later, the population inversion disappears and the Stokes component is enhanced due to the lasing without inversion (LWI) [11]. Thus, the lasing on the Stokes component is induced by the ASE, which is followed later by the LWI. Both of these processes are manifestations of the general process SRRS. The SRRS spectrum differs from the spectrum of the spontaneous resonant x-ray Raman scattering [12,13]. The simulations show the compression of the pulse (up to 100 as) which depends strongly on the area, duration, and shape of the pulse and the geometry of light propagation. Such ultrashort x-ray pulses are needed to probe electronic processes, many of which take place in the attosecond time domain [14].

Our theoretical model is based on the strict numerical solution of the coupled Bloch and Maxwell equations for three-level atoms. We consider two geometries of pulse propagation. The first one is a linear geometry, which ignores the transverse inhomogeneity of the light; the second one, a so-called focusing geometry, models the focusing of the light using a uniform spherical propagating wave. The linear geometry shows that the compression of the pulse is about 5–10 times, while the focusing geometry can give 20-fold pulse compression. Special attention is paid to the spectrum of the generated field, which consists of four coherent bands caused by the pump radiation and the Stokes component, as well as the Stokes and the anti-Stokes sidebands induced by four-wave mixing. These spectral bands display fine structures caused by the dynamical Stark effect.

The article is organized as follows. We start with the outline of the theoretical model for the linear geometry (Sec. II). We also model the role of focusing of the pulse by solving Maxwell's equations for uniform spherical propagating waves. Details of the numerical scheme are described in Sec. III. Section IV is devoted to discussions of the obtained results. Our findings are summarized in the last section, Sec. V.

---

[*] jicai@theochem.kth.se

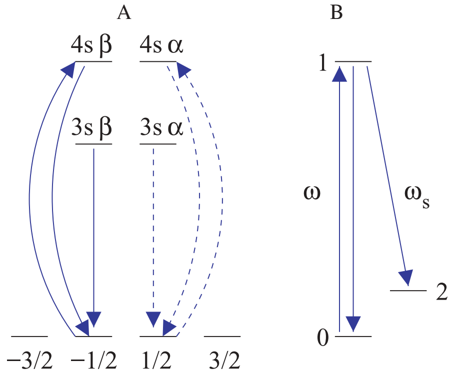

FIG. 1. (Color online) Scheme of transitions, where $m = \pm 3/2, \pm 1/2$ is the projection of the total momentum of the $2p_{3/2}$ core level. $|1\rangle = |2p_{3/2}^{-1}4s\rangle$, $|2\rangle = |3s^{-1}4s\rangle$.

II. MODEL

We consider the interaction between three-level atoms (Fig. 1) and x-ray pulses. The total electric field $E(t, y)$ includes all fields, namely the incident x-ray field, as well as the fields generated during pulse propagation. Apparently, the generated fields have the same polarization vector as the incident pulse because the origin of these fields is the stimulated emission or scattering. Due to the spherical symmetry of atoms, the choice of the quantization axis z is not important. We orient z along the polarization vector $\mathbf{e}$ of the linearly polarized field. The prototype system is the L_{III} ($2p_{3/2} \to 4s$) absorption transition in an Ar atom followed by the ($4s \to 2p_{3/2}, 3s \to 2p_{3/2}$) emission transitions. We have two independent scattering channels [Fig. 1(A)],

$$\begin{aligned} &2p_{3/2,1/2} \to 4s\alpha,\ ns\alpha \to 2p_{3/2,1/2} \\ \text{and}\quad &2p_{3/2,-1/2} \to 4s\beta,\ ns\beta \to 2p_{3/2,-1/2}, \end{aligned} \tag{1}$$

because in the frame with $\mathbf{e} \parallel z$ only the transition dipole moments

$$\langle 2p_{3/2,1/2}|z|ns\alpha\rangle = \langle 2p_{3/2,-1/2}|z|ns\beta\rangle = \sqrt{\frac{2}{3}}d_{2p,ns} \tag{2}$$

are not equal to zero. Here $n = 3, 4$. $2p_{3/2,m}$ means the wave function of the L_{III} level with the projection of the total momentum $m = \pm 3/2, \pm 1/2$, α and β are the spin wave functions with the momentum $1/2$ and $-1/2$, respectively, and $d_{2p,ns} = \langle 2p|z|ns\rangle$. This means that one can consider only one of the channels (1) with the transition dipole moments $d_{10} = d_{2p,4s}\sqrt{2/3}$, $d_{21} = d_{2p,3s}\sqrt{2/3}$. Thus, we study the three-level system [Fig. 1(B)]: The ground state $|0\rangle$, core-excited state $|1\rangle = |2p_{3/2}^{-1}4s\rangle$, and two final states, $|0\rangle$ and $|2\rangle = |3s^{-1}4s\rangle$.

The frequency of the incident light ω is assumed to be in resonance with the x-ray absorption transition $0 \to 1$. The population of the core-excited state generates new fields related to the decay transitions $1 \to 0$ and $1 \to 2$.

To describe the pulse propagation along the y axis, we solve numerically the coupled Bloch [15],

$$\begin{aligned} &\left[\frac{\partial}{\partial t} + \Gamma + \gamma_{ph}^{(1)}(t)\right]\rho_{11} = W \equiv 2\ \mathrm{Im} \sum_{n=0,2} (V_{1n}\rho_{n1}e^{\imath\omega_{1n}t}), \\ &\quad V_{nm} = -E(t, y)d_{nm}/\hbar \end{aligned}$$

$$\begin{aligned} &\left[\frac{\partial}{\partial t} + \Gamma_f + \gamma_{ph}^{(2)}(t)\right]\rho_{22} = 2\ \mathrm{Im}\,(V_{21}\rho_{12}e^{-\imath\omega_{12}t}), \\ &\frac{\partial}{\partial t}(\rho_{00} + \rho_{11} + \rho_{22}) \\ &\quad = -\left[\Gamma + \gamma_{ph}^{(1)}(t)\right]\rho_{11} - \left[\Gamma_f + \gamma_{ph}^{(2)}(t)\right]\rho_{22} - \gamma_{ph}^{(0)}(t)\rho_{00}, \\ &\left\{\frac{\partial}{\partial t} + \gamma + \frac{1}{2}\left[\gamma_{ph}^{(1)}(t) + \gamma_{ph}^{(0)}(t)\right]\right\}\rho_{10} \\ &\quad = \imath V_{10}(\rho_{11} - \rho_{00})e^{\imath\omega_{10}t} - \imath V_{12}\rho_{20}e^{\imath\omega_{12}t}, \\ &\left\{\frac{\partial}{\partial t} + \gamma + \gamma_f + \frac{1}{2}\left[\gamma_{ph}^{(1)}(t) + \gamma_{ph}^{(2)}(t)\right]\right\}\rho_{12} \\ &\quad = \imath V_{12}(\rho_{11} - \rho_{22})e^{\imath\omega_{12}t} - \imath V_{10}\rho_{02}e^{\imath\omega_{10}t}, \\ &\left\{\frac{\partial}{\partial t} + \gamma_f + \frac{1}{2}\left[\gamma_{ph}^{(0)}(t) + \gamma_{ph}^{(2)}(t)\right]\right\}\rho_{20} \\ &\quad = -\imath V_{21}\rho_{10}e^{-\imath\omega_{12}t} + \imath\rho_{21}V_{10}e^{\imath\omega_{10}t}, \end{aligned} \tag{3}$$

and 1D Maxwell's equations (linear geometry),

$$\frac{\partial E}{\partial y} + \mu_0\frac{\partial H}{\partial t} = 0, \qquad \frac{\partial H}{\partial y} + \epsilon_0\frac{\partial E}{\partial t} = -\frac{\partial P}{\partial t}, \tag{4}$$

which ignore the transverse inhomogeneity of the pulse. We use the SI units. The Maxwell's equations take into account all fields generated in the medium through the light-induced polarization

$$P(t, y) = N\ \mathrm{Tr}(d\rho) = 2N\ \mathrm{Re}\,(d_{10}\rho_{01}e^{\imath\omega_{10}t} + d_{12}\rho_{21}e^{\imath\omega_{12}t}). \tag{5}$$

Here $\omega_{mn} = (E_m - E_n)/\hbar$ are the resonant frequencies, $E \equiv E_z$, $H \equiv H_x$, and N is the concentration of the atoms. The density matrix ρ is normalized to one for $t \leqslant 0$. It is necessary to note that the total number of resonant atoms (3) $\rho_{00} + \rho_{11} + \rho_{22}$ decreases for $t > 0$ because of the Auger decay (we neglect possible recombination process) and direct ionization. Equations (3) and (4) are coupled with each other through the interaction V and the polarization $P(t, y)$. The total field $E(t, y)$ now includes the input pulse with the envelope $\mathcal{E}(t, y)$, as well as all other fields, which are generated during pulse propagation. We assume in Maxwell's equations that the effect of backward-traveling waves is negligible. Usually the role of backward waves is rather weak [16].

The major channel of ionization for the studied system is the Auger decays of the core-excited and the final states with the relaxation rates Γ and Γ_f, respectively. We neglect the spontaneous decay rate because it is much smaller in comparison with Γ. However, the XFEL pulse can ionize also the $3s$ and $3p$ electrons when the intensity is high enough. This direct ionization depopulates electronic states with the photoionization rates

$$\gamma_{\mathrm{ph}}^{(k)}(t) = \sigma_k s(t), \qquad k = 0, i, f. \tag{6}$$

Here σ_k is the photoionization cross section in the state k, $s(t) = I(t)/\hbar\omega$ is the photon flux, while $I(t) = |E(t)H(t)|$ is the intensity, which is an absolute value of the Poynting vector. The coherences ρ_{10}, ρ_{12}, and ρ_{20} decay with the rates $\gamma + [\gamma_{\mathrm{ph}}^{(0)}(t) + \gamma_{\mathrm{ph}}^{(1)}(t)]/2$, $\gamma + \gamma_f + [\gamma_{\mathrm{ph}}^{(1)}(t) + \gamma_{\mathrm{ph}}^{(2)}(t)]/2$, and $\gamma_f + [\gamma_{\mathrm{ph}}^{(0)}(t) + \gamma_{\mathrm{ph}}^{(2)}(t)]/2$, respectively, where $\gamma = \Gamma/2$, $\gamma_f = \Gamma_f/2$.

One of the aims of our study is the pulse reshaping in the course of propagation, especially its compression. The compression for the linear geometry considered earlier in this article is limited, as we will see in Sec. IV. The focusing geometry can make the compression stronger [17]. Strict treatment of focusing requires the solution of 2D Maxwell's equations (y, r). Instead of this, we follow the simplified 1D model suggested by Gibbs and Slusher [17] based on the converging spherical wave which propagates along the r axis, $\mathbf{k} \parallel r$. Using the spherical coordinates (r, ϑ, φ), let us choose $\mathbf{E} = (0, 0, E)$, $\mathbf{P} = (0, 0, P)$, $\mathbf{H} = (0, H, 0)$. Thus, the focusing model used is described by the following Maxwell's equations

$$\frac{\partial E}{\partial r} + \frac{E}{r} - \mu_0 \frac{\partial H}{\partial t} = 0, \qquad \frac{\partial H}{\partial r} + \frac{H}{r} - \epsilon_0 \frac{\partial E}{\partial t} = \frac{\partial P}{\partial t}. \tag{7}$$

The applicability of the linear and focusing geometries depends on the experimental conditions, namely, the focal length and the concentration of the atoms. A focal length (f) ranging from 0.1 to 10 m is technically feasible [18]. The 1D model based on the linear geometry is working well when the concentration is high enough to make the propagation distances below 0.1 m. The role of focusing of the x-ray beam becomes important for propagation distances comparable with the focal length. For example, it occurs at concentrations less than 10^{18} cm^{-3} if $f \sim 0.1$ m.

III. OUTLINE OF THE SIMULATIONS

The Bloch and Maxwell equations are solved by an iterative predictor-corrector finite-difference time-domain (FDTD) method [19] with the steps of integration $\delta t = 2\pi/120\omega$, $\delta y = 2c\delta t$. We use the experimental frequencies $\omega = \omega_{10} = 244.3$ eV [20], $\omega_{12} = 219.28$ eV [21], and $\Gamma = 0.12$ eV full width at half maximum (FWHM) [20,22]. We do not know the Auger rate of the final state $|2\rangle = |3s^{-1}4s\rangle$. However, it is natural to assume that this Auger rate is close to the lifetime broadening of the $|3s^{-1}4p\rangle$ state 0.076 eV [23]. Thus, we use $\Gamma_f \approx 0.076$ eV in the calculations. The transition dipole moment $d_{10} = \sqrt{137\sigma_{10}\Gamma/(8\pi\omega)} = 0.137$ a.u. is calculated using the experimental cross section $\sigma_{10} \approx 2$ Mb [24,25] and $d_{21} = d_{10} d_{21}^{\text{theo}}/d_{10}^{\text{theo}} = 0.322$ a.u. is obtained by rescaling the theoretical value d_{21}^{theo}. One should note that the theoretical transition dipole moments $d_{10}^{\text{theo}} = 0.0204$ a.u. and $d_{21}^{\text{theo}} = 0.048$ a.u. are smaller than the experimental values because the interaction with the core hole is neglected in the *ab initio* calculations [26]. We use in the simulations the experimentally defined values for the transition dipole moments $d_{10} = 0.137$ a.u. and $d_{21} = 0.322$ a.u. to make the calculations closer to the real system.

The envelope of the input pulse $E_0(t, y) = \mathcal{E}(t, y)\cos(\omega t - ky)$ in linear geometry (4) is modeled in the simulations by sech and Gaussian shapes

$$\begin{aligned} \mathcal{E}(t, y) &= \mathcal{E}_0 \ \text{sech}\left(\frac{t - y/c - t_0}{\tau'}\right), \\ \mathcal{E}(t, y) &= \mathcal{E}_0 \ \exp\left[-2\ln 2\left(\frac{t - y/c - t_0}{\tau}\right)^2\right]. \end{aligned} \tag{8}$$

Here $k = \omega/c$, $t_0 = 20\tau'$, $\tau' = \tau/1.76$, and τ is the FWHM of the pulse intensity. The initial amplitude of the electric field $\mathcal{E}_0$ corresponds to the initial peak intensity $I_0 = c\varepsilon_0\mathcal{E}_0^2/2$. The major part of the simulations are performed for the Gaussian pulse, which is closer to the experimental XFEL profile. We put the beginning of the medium at $y = 0$, assuming $y \geqslant 0$. The initial shape of the pulse for the focusing geometry (7) is the same as (8), except for the coordinate y, which has to be replaced by $y \to \Delta r \geqslant 0$. The pulse travels from the outer sphere with the radius R to the inner sphere with $r = R - \Delta r > 0$, where r is the radial distance from the focal point.

Our simulations are performed for a high concentration of the argon atoms $N = 2.23 \times 10^{21}$ cm^{-3} only to avoid the large propagation distances. Such a high concentration results in a broadening of the spectral line, which is ignored in our simulations. This means that our simulations are valid for the gas phase. However, it is easy to get results for a lower concentration N' by replacing the propagation length y (or Δr),

$$y' = y\frac{N}{N'}, \tag{9}$$

and the time $t' = T \mp y'/c$ keeping the same local time T. Such a scaling follows directly from the wave equation for the envelope of the electromagnetic field equations in the local frame (T, y),

$$\frac{\partial \mathcal{E}(T, \tilde{y})}{\partial \tilde{y}} = \pm\frac{\imath}{2}\mu_0 c\omega \mathcal{P}(T, \tilde{y}). \tag{10}$$

The only change of the Bloch equations (3) in this frame is $t \to T$. Here $\tilde{y} = yN$, $T = t \pm y/c$. To get this equation we used the slowly varying envelope approximation to the field

$$E = \frac{\mathcal{E}}{2}e^{\imath\omega T} + \text{c.c.}, \qquad P = N\frac{\mathcal{P}}{2}e^{\imath\omega T} + \text{c.c.},$$

which is valid in our case because of the high frequency of the x-ray photons.

Our numerical simulations assume a fully coherent x-ray pulse. Different schemes to get such pulses have been suggested previously (see [27–29] and references therein). For example, a fully coherent XFEL pulse can be obtained using self-seeding or single-pass two-stage x-ray self-amplified spontaneous emission [27–29].

IV. DISCUSSION

To give insight into the physics, it is instructive to neglect for a while the 1-2 channel and the direct ionization $[\gamma_{\text{ph}}^{(k)}(t) = 0]$. The input pulse populates the core-excited state $\rho_{11}(t) = \sin^2[\theta(t)/2]$ according to the area of the pulse $\theta \equiv \theta(\infty)$, where

$$\theta(t) = \frac{d_{10}}{\hbar}\int_{-\infty}^{t} \mathcal{E}(t_1, y)dt_1. \tag{11}$$

We study later in this article the pulses with the input area $\theta \geqslant \pi$. These pulses create the inversions between the core-excited and ground states and between the core-excited and final states (Fig. 1). This means that the propagation of the x-ray pulse can be followed by ASE from two channels, 1-0 and 1-2. Due to these two competing ASE channels, one can expect the reshaping of the pulse during propagation, as well as a change of its spectrum. However, we will see that the ASE is followed by the LWI, which is important in the formation of the Stokes band near ω_{12}. The spectrum of the generated field consists also of weaker anti-Stokes and Stokes components caused by four-wave mixing.

We would like to pay attention to one qualitative difference between the propagation of x-ray and optical pulses. The dynamics of the latter one is strongly affected by the inhomogeneous broadening (for example Doppler broadening). This type of broadening is absent in our case, and hence the x-ray pulse area for two-level atoms obeys the sine-Gordon equation [30] instead of the McCall-Hahn equation [31]. This results in a rather distinct dynamics of the x-ray pulse [30,32].

A. Linear geometry

1. *π pulse: self-seeding*

Let us analyze the solution of the Bloch and Maxwell equations for the pulse propagation along the y axis and start from the propagation of the π x-ray pulse (see Fig. 2), which inverts the medium. This results in a formation of the time-delayed ASE 1-0 and 1-2. The front of the π pulse is deformed and attenuated during propagation. Already for the two-level system [$d_{12} = 0$, Fig. 2(B)] we see the formation of the ringing structure during propagation, which is nothing other than the Burnham-Chiao (BC) ringing [30,33],

$$\mathcal{E} \propto J_0(\zeta) \approx \sqrt{2/(\pi\zeta)}\cos(\zeta - \pi/4), \quad \zeta \gg 1. \tag{12}$$

This equation shows the gain in an inverted medium and the sign-changing modulation of the envelope in the region where the inversion is absent. Here $J_0(x)$ is the Bessel function and $\zeta = 2|y(t - y/c)N(\rho_{00} - \rho_{11})kd_{10}^2/(2\hbar\varepsilon_0)|^{1/2}$.

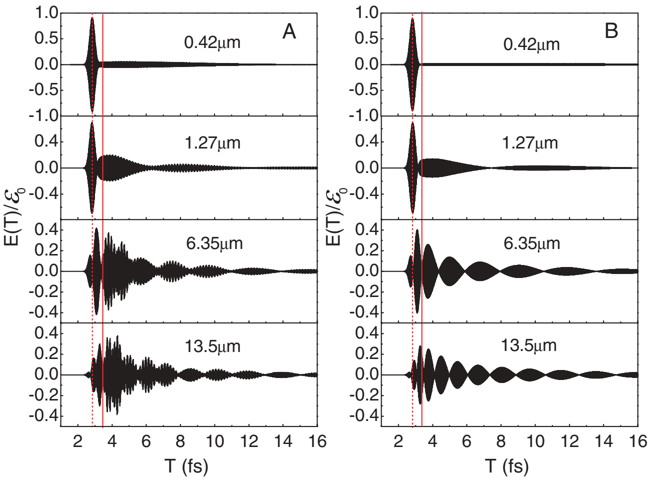

FIG. 2. (Color online) Linear geometry. Gaussian π pulse. $\tau = 0.25$ fs. The fine structure of the temporal shape of the pulse for different propagation lengths $y = 0.42$–13.5 μm versus the local time $T = t - y/c$. (A) Three-level model. The spacing of the beating $\Delta t = 2\pi/(\omega_{10} - \omega_{12}) = 0.17$ fs. (B) Two-level model. $\mathcal{E}_0 = 7.76 \times 10^9$ V/cm, $I_0 = 7.98 \times 10^{16}$ W/cm^2, the photon flux $s_0 = 2.04 \times 10^{33}$ photon/(cm^{2}s).

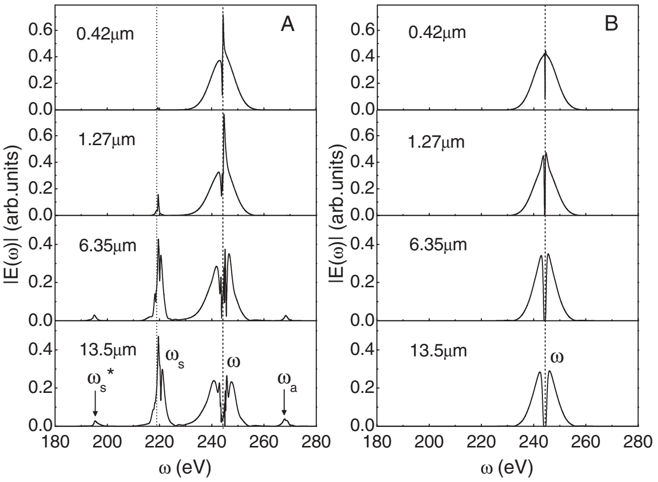

FIG. 3. Linear geometry. Gaussian π pulse. $\tau = 0.25$ fs. The spectrum $|E(\omega)|$ of the whole pulse shown in Fig. 2 for different propagation lengths y. (A) Three-level model, (B) two-level model. Panel (A) displays two strong bands near the pump (ω) and Stokes (ω_s) frequencies as well as two weaker anti-Stokes (ω_a) and Stokes (ω_s^*) components caused by four-wave mixing [see Eq. (14)].

Let us now look at the x-ray pulse propagation through the herein-studied three-level system. The first impression is that the difference between the two- and three-level solutions must be small due to the large spacing between states 0 and 2 (about 25 eV). However, Fig. 2 shows that this expectation is failed, because the two- and three-level media reshape the XFEL pulse differently. The spectral analysis shows that only the front part of the pulse [before solid line in Fig. 2(A)] is the same and it consists only of the pump component $\omega = \omega_{10} = 244.3$ eV, while the rest of the pulse is formed by coherent pump ω and Stokes ($\omega_s \approx \omega_{12} = 219.28$ eV) components. Due to this, the total field experiences the beating [Fig. 2(A)] with the spacing,

$$\Delta t = 2\pi/(\omega_{10} - \omega_{12}) = 0.17 \text{ fs}, \tag{13}$$

much smaller than the characteristic time of the BC ringing [Fig. 2(B)]. At the beginning of the medium one can see mainly the radiation near pump frequency ω_{10} (Fig. 3). For larger y we start to see the 1-2 Stokes band which grows during propagation. We would like to pay attention to the fine structure seen near the ω_{10} and ω_{12} bands. The splitting of the ω_{10} is seen clearly. The spectrum for the two-level system is rather similar, except that the ω_{12} band is absent [Fig. 3(B)]. The origin of splitting of the ω_{10} band is the Rabi splitting. Indeed, the splitting $\Delta E = 2.50$ eV for the two-level system [Fig. 3(B)] at $y = 6.35$ μm is rather close to the Rabi splitting $\hbar G = \mathcal{E}_0' d_{10} = 1.51$ eV, where $\mathcal{E}_0'$ corresponds to the maximum of the second bunch in Fig. 2(B). Figure 3 shows the appearance of two weak sidebands,

$$\begin{aligned} \omega_a &= 2\omega - \omega_s \approx 2\omega_{10} - \omega_{12}, \\ \omega_s^* &= 2\omega_s - \omega \approx 2\omega_{12} - \omega_{10}, \end{aligned} \tag{14}$$

which grow during propagation. The origin of these anti-Stokes and Stokes components is the four-wave mixing [34] shown schematically in Fig. 4. The calculations show that pulses with areas different from π and 3π also generate these fields.

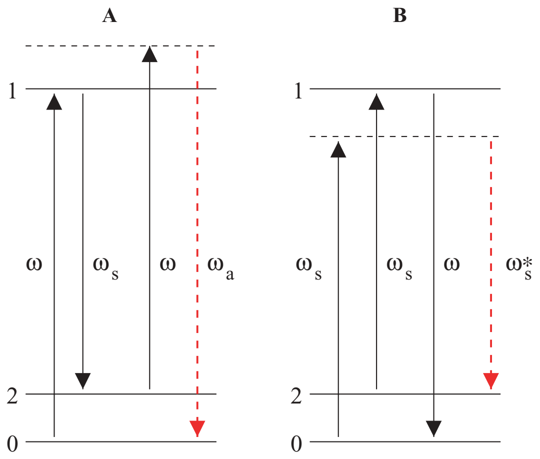

FIG. 4. (Color online) Scheme of generation of the anti-Stokes (A) and Stokes (B) fields (dashed red line) caused by the coherent four-wave mixing [see Eq. (14)].

During propagation the front part of the pulse is attenuated up to zero (Fig. 2). The energy of the pulse is transferred to the medium creating the inversion. The inversion $\rho_{11} - \rho_{00}$ exists until $y = y_c \approx 1.5\ \mu$m. Later, the inverted medium returns the energy to the field by emitting the time-delayed ASE which forms the BC ringing. In fact, we see the significant population of the core-excited level 1 only at the beginning of the medium ($<2.54\ \mu$m). Here at the front of the pulse we see the inversion $\rho_{11} - \rho_{22}$ which leads to the 1-2 ASE. For larger distances the inversion $\rho_{11} - \rho_{22}$ is absent. The main reason for this is the BC sign-changing oscillations of the field envelope. Indeed, the same quenching of the inversion is seen also for the two-level system. This means that the ASE is the main mechanism of the enhancement of the Stokes 1-2 light for the distances $<2.54\ \mu$m. The enhancement of the 1-2 component for larger distance is mainly because of the LWI which does not need the inversion. The ASE channel 1-2 followed by the LWI starts from the seed radiation near the Stokes band ω_{12}. The Fourier transform

$$\begin{aligned} E(\omega) &= \mathcal{E}_0 \pi\tau' \mathrm{sech}[\pi\tau'(\omega - \omega_{10})/2], \\ E(\omega) &= \mathcal{E}_0 \sqrt{\pi}\,\tau_0 \exp\{-[(\omega-\omega_{10})\tau_0/2]^2\} \end{aligned} \tag{15}$$

of the input field $E_0(t)$ (8) says that when $\tau = 0.25$ fs, $|E(\omega_{12})/E(\omega_{10})|^2 \approx 1.71 \times 10^{-7}$ for the sech pulse and $|E(\omega_{12})/E(\omega_{10})|^2 \approx 0.71 \times 10^{-14}$ for the Gaussian input pulse. Here $\tau_0 = \tau/\sqrt{2\ln 2}$. The first impression is that the Gaussian input pulse does not give large enough seed radiation to generate the SRRS. However, this impression is incorrect. The calculations show that the development of the Stokes field for the input Gaussian pulse (Fig. 3) is very close to the input sech pulse (which is not shown here). This is because during propagation the temporal shape of the initial Gaussian pulse changes, and this gives enough seed light to generate the Stokes component.

To check this idea, we perform simulations of pulse propagation in the two-level medium for the sech and Gaussian input pulses. The two-level system is chosen to be sure that the seed radiation near the Stokes band $\omega_s \approx 219.28$ eV is not due to the SRRS process. One can see that the Fourier transform $E(\omega)$ for both pulses consists of the central part and long weak tail (Fig. 5). The central part of the Gaussian input pulse becomes wider, contrary to that seen with the sech pulse. The comparison of the spectral distributions $E(\omega)$ at $y = 0$ (15) and $y = 1.27\ \mu$m shows unambiguously that during propagation the intensity of the input Gaussian pulse (near the Stokes line $\omega_s \approx 219.28$ eV) becomes much higher than that at the entry in the medium, $y = 0$ [see Fig. 5(A)]. This enhancement of the intensity of the pulse near the Stokes band results in an self-seeding mechanism of the SRRS in the three-level medium. The spectral reshaping of the Gaussian pulse deserves a special comment. Figure 5 shows that the pulse propagation leads to the broadening of the central part of $E(\omega)$ and formation of the weak long tail. The origin of the spectral broadening is the BC modulation (12) itself, while the spectral tail is due to the decrease of the BC pattern $\mathcal{E} \propto t^{-1/4}$ [see Eq. (12) and Fig. 2]. The latter results in a weakly decaying tail in the Fourier transform $E(\omega) \propto (\omega - \omega_{10})^{-3/4}$. Simulations show that the spectral tail approximately follows this power law.

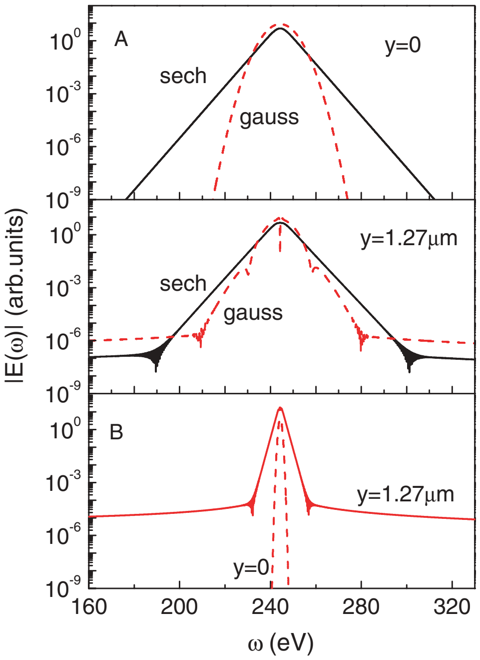

FIG. 5. (Color online) The self-seeding. The development of the spectral shape of the XFEL pulse during the propagation in the two-level medium. Linear geometry. (A) $\theta = \pi$; $\tau = 0.25$ fs. The inputs are sech (solid line) and Gaussian pulses (dashed red line). (B) $\theta = 3\pi$; $\tau = 2$ fs. The input is a Gaussian pulse. $y = 0$ (dashed red line); $y = 1.27\ \mu$m (solid red line).

2. *3π pulse*

We now turn to the propagation of the 3π input sech and Gaussian pulses. This case is interesting because in the case of the two-level system the 3π pulse inverts the medium. We perform simulations for the pulse durations $\tau = 0.25$ fs, 2 fs, 4 fs $< 1/\Gamma = 5.5$ fs. The results of calculations of the 0.25- and 4-fs pulses are only discussed here, without showing the figures. The simulations show small compression for the short pulses ($\tau = 0.25$ fs): The input sech and Gaussian

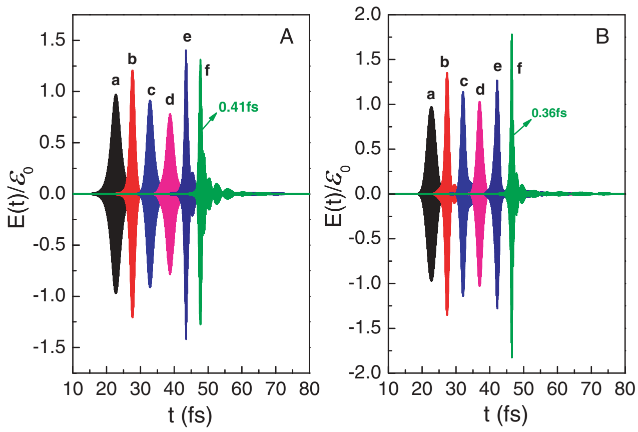

FIG. 6. (Color online) Linear geometry. $\theta = 3\pi$; $\tau = 2$ fs. The temporal shapes of the pulse for different propagation lengths $y = 0,\ 1.27,\ 2.54,\ 3.81,\ 5.08$, and $6.35\ \mu$m are marked by the labels a, b, c, d, e, and f, respectively. (A) Sech pulse. $\mathcal{E}_0 = 2.45 \times 10^9$ V/cm, $I_0 = 7.98 \times 10^{15}$ W/cm^2, the photon flux $s_0 = 2.04 \times 10^{32}$ photon/(cm^{2}s). (B) Gaussian pulse. $\mathcal{E}_0 = 2.91 \times 10^9$ V/cm, $I_0 = 1.12 \times 10^{16}$ W/cm^2, the photon flux $s_0 = 2.85 \times 10^{32}$ photon/(cm^{2}s). The 0.41 fs and 0.36 fs mean FWHMs of the intensity distributions of corresponding pulses.

pulses are compressed up to 0.13 and 0.11 fs, respectively. The compression of the longer input pulse $\tau = 4$ fs is seen only for the Gaussian pulse. This compression is also not strong (2.2 fs at $y = 1.27\ \mu$m). The reason for the compression is the intrinsic chirp produced in the course of propagation. To give insight into the physics of the pulse reshaping (Fig. 6), let us analyze the spectrum (Fig. 7) and the population inversion (Fig. 8) for the $\tau = 2$-fs pulse which experiences strong compression (FWHM = 0.36 fs).

First of all, we pay attention to the compression of the pulse which is stronger for the Gaussian input pulse (Fig. 6). The second interesting result is the Stokes component which is seen for both pulse shapes (Fig. 7). The appearance of the Stokes component for Gaussian pulses is somehow unexpected because the seed radiation created by the 2-fs pulse near ω_{12} is negligibly small at the entry ($y = 0$) according to Eq. (15) and Fig. 5(B). However, as it was shown above the seed radiation arises during the pulse propagation. Contrary to the 0.25-fs pulse, the source of the seed field is now the tail of $E(\omega)$ which is much stronger than the field caused by the spectral broadening of the central part [compare Figs. 5(A) and 5(B)]. One should notice that the role of this spectral tail is crucial for the self-seeded formation of the Stokes field for longer input pulses $\tau = 4$, 6 fs.

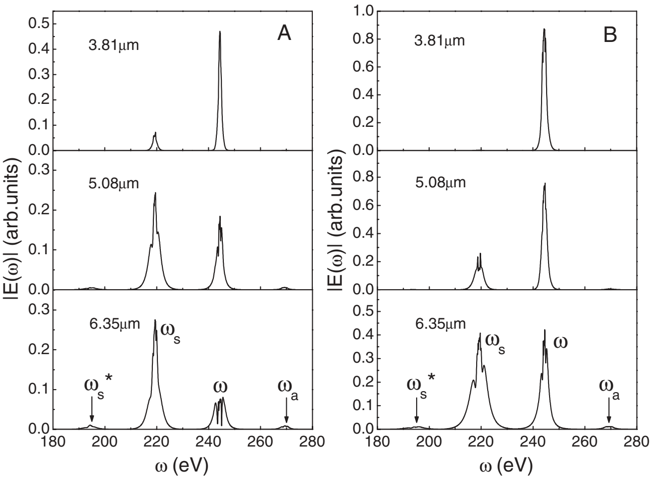

FIG. 7. Linear geometry. $\theta = 3\pi$; $\tau = 2$ fs. The spectrum $|E(\omega)|$ of the whole pulse for the propagation lengths $y = 3.81$, 5.08, and $6.35\ \mu$m shown in Fig. 6. (A) Sech pulse. (B) Gaussian pulse. The spectrum consists of two strong bands near the pump (ω) and Stokes (ω_s) frequencies, as well as two weaker anti-Stokes (ω_a) and Stokes (ω_s^*) components caused by four-wave mixing [see Eq. (14)].

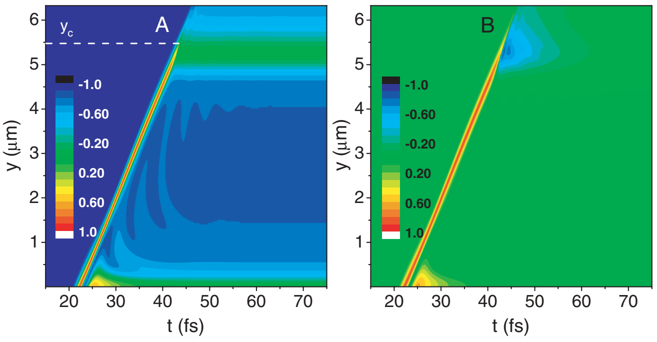

FIG. 8. (Color online) Linear geometry. $\theta = 3\pi$; $\tau = 2$ fs. Gaussian pulse. The 2D maps of the population inversions, which are quenched in the region $y > y_c$. (A) $\rho_{11}(t,y) - \rho_{00}(t,y)$, (B) $\rho_{11}(t,y) - \rho_{22}(t,y)$. The parameters are the same as in Fig. 6.

It should be pointed out that Fig. 6 shows the temporal profile of the whole spectral band (Fig. 7). Hence, this profile corresponds to energy unresolved measurements. However, one can detect separately the spectral band near the pump frequency ω and the Stokes band ($\approx \omega_s$) (or spectral bands of four-wave mixing). The natural question arises: What temporal shapes correspond to each of these spectral bands? To get the answer, let us perform the inverse Fourier transform $E(\omega) \rightarrow E(t)$ for each spectral band. As expected, these pulses have different shapes. Figure 9 shows the temporal profiles at $y = 6.35\ \mu$m for the band near the pump frequency ω and the Stokes band. One can see that the Stokes band is compressed more strongly (FWHM = 0.31 fs) than the ω band (0.57 fs). The total profile [Fig. 6(B)] is slightly broader (0.36 fs) in comparison with the Stokes pulse. It is worth noting that the compression effect does not depend on the concentration N because the scaling (10) does not change the local time T.

Let us now pay attention to the population inversions (Fig. 8), which are important for the competition between ASE and LWI processes. One can see that both inversions $(\rho_{11} - \rho_{00})$ and $(\rho_{11} - \rho_{22})$ exist until the critical distance $y_c \approx 5.5\ \mu$m. The inversions are suddenly quenched for $y > y_c$. The reason for such abrupt quenching is the field work W [see Eq. (3)], which is responsible for the population of the core-excited state,

$$\rho_{11}(t,y) = \int_{-\infty}^{t} e^{-\Gamma(t-t_1)} W(t_1,y)\,dt_1. \tag{16}$$

Figure 10A shows that when $y < y_c$ the field work changes sign near the pulse maximum. The positive (intense and broad) part W_A of W at the pulse front creates large population ρ_{11} and, hence, the inversions (Fig. 8). Then the absorption is

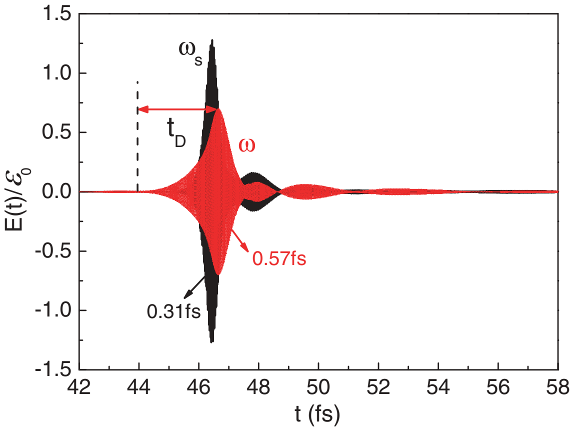

FIG. 9. (Color online) The temporal shapes of the pulses which correspond to the spectral band near pump frequency ω [red (light gray) line] and to the Stokes band near ω_s [black (dark) line] [Fig. 7(B)] at $y = 6.35$ μm. Linear geometry. Gaussian pulse $\theta = 3\pi$; $\tau = 2$ fs [see Fig. 6(B)]. The time delay $t_D \approx 2.68$ fs.

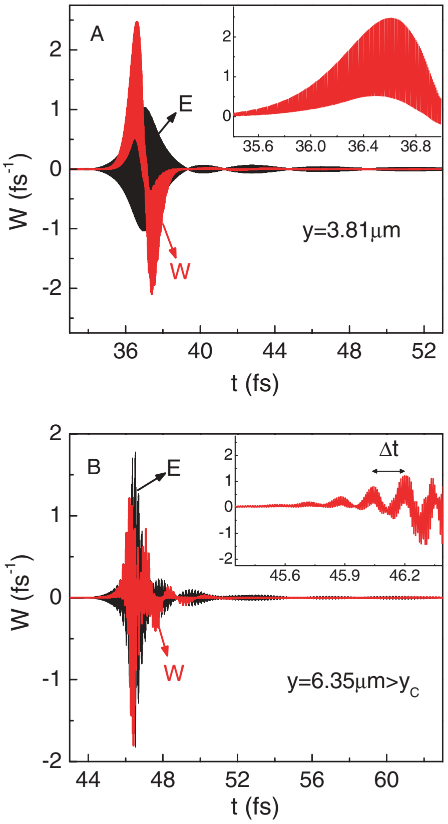

FIG. 10. (Color online) Linear geometry. $\theta = 3\pi$; $\tau = 2$ fs. The field work W (3) [red (light gray) line] for the Gaussian pulse. The parameters are the same as in Fig. 6. The pulse is shown by a black (dark) line. The insets display W before the pulse maximum. $\Delta t = 0.17$ fs (13). (A) $y = 3.81$ μm $< y_c$. (B) $y = 6.35$ μm $> y_c$.

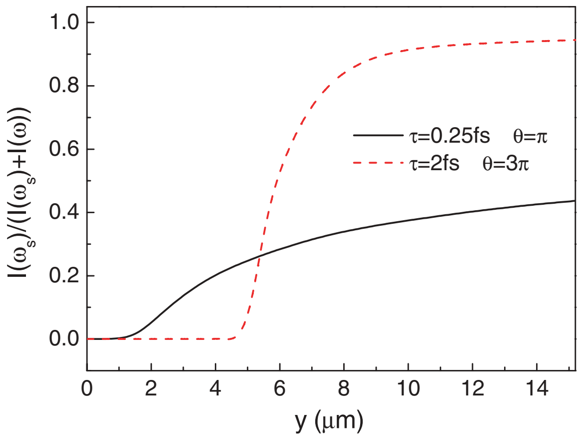

FIG. 11. (Color online) Stokes branching ratio (17) for $\theta = \pi$ ($\tau = 0.25$ fs) and 3π ($\tau = 2$ fs). Linear geometry.

followed by the stimulated emission ($W = -W_E < 0$), which depopulates the upper state. The picture changes qualitatively for $y > y_c$, where the Stokes field becomes comparable with the pump radiation and the field work experiences fast sign-changing oscillations with the frequency $\omega - \omega_s \approx \omega_{20} = 25$ eV [see Fig. 10(B)]. These fast oscillations of W prevent significant population of the core-excited state. This is attributed to the small area of each positive narrow spike W_A and hence small population $\rho_{11} \approx \int W_A(t_1, y)dt_1$. Thus, the ASE process is the major reason of the pulse reshaping at the beginning of the medium. This process being important in the inverted region $y \lesssim y_c$ triggers the Stokes ASE channel $1 \to 2$. We see also the lasing in the region $y \gtrsim y_c$, where the inversions are absent (compare Figs. 8 and 7). It should be mentioned that the LWI process is stronger ($y > y_c$) than the ASE 1-2 channel ($y < y_c$). This is because the 1-0 ASE triggered by the strong pump field blocks the 1-2 ASE which needs the seed radiation. The simulations show that the Stokes component in the spectrum becomes comparable to or even larger than the main line when $y > y_c$. Having seen the amplification of the Stokes field, one should ask about this field at longer distances. Figure 11 shows the development of the Stokes branching ratio,

$$\frac{I(\omega_s)}{I(\omega_s) + I(\omega)}, \tag{17}$$

during propagation. Here $I(\omega) \propto \int |E(\omega')|^2 d\omega'$ is the integral intensity of the bands near the Stokes ω_s and pump ω frequencies. One can see the saturation of the Stokes component at longer propagation distances.

3. 2.5π, 3.5π pulses

To get strict π or 3π pulses is not an easy experimental task. This motivates us to explore the role of the pulse area on the compression effect and on the spectrum. Figure 12 shows the results of simulations for intermediate input areas $\theta = 2.5\pi$ and 3.5π of the 2-fs input pulse. The compression (0.41 fs for 2.5π and 0.51 fs for 3.5π) is slightly weaker than for 3π pulse. The pulse area affects strongly the spectrum. The 2.5π pulse has rather weak Stokes component, contrary to the 3.5π (Fig. 12) and 3π pulses (Fig. 7).

B. Group velocity

Röntgen faced the problem of how to reflect and focus x-rays with mirrors and lenses of various materials. The reason for his lack of success became evident after it was established

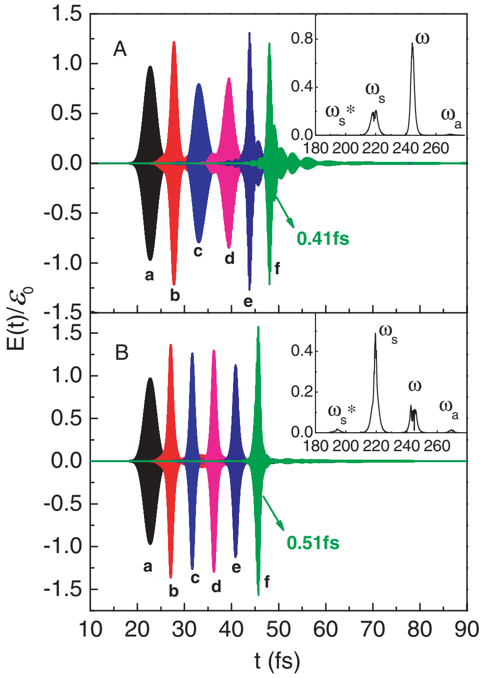

FIG. 12. (Color online) Linear geometry. Gaussian $\tau = 2$-fs input pulse. The temporal shapes of the pulse for $y = 0$, 1.27, 2.54, 3.81, 5.08, and 6.35 μm are marked by the labels a, b, c, d, e, and f, respectively. The insets are the spectrum at $y = 6.35$ μm. (A) $\theta = 2.5\pi$, $\mathcal{E}_0 = 2.41 \times 10^9$ V/cm, $I_0 = 7.77 \times 10^{15}$ W/cm^2, the photon flux $s_0 = 1.99 \times 10^{32}$ photon/(cm^{2}s). (B) $\theta = 3.5\pi$, $\mathcal{E}_0 = 3.39 \times 10^9$ V/cm, $I_0 = 1.53 \times 10^{16}$ W/cm^2, the photon flux $s_0 = 3.90 \times 10^{32}$ photon/(cm^{2}s).

that the x-ray refractive index $n_0 = 1 - \delta$ of all materials is smaller than unity by only a small decrement $\delta < 10^{-4}$. This makes the propagation of x-rays with low intensities in different media with the speed c/n_0 very close to the speed of the light in vacuum c. In connection with this, Fig. 13 shows an unexpected result for the x-ray region. One can see a strong deviation of the XFEL pulse trajectory from the straight line $y - c(t - t_0)$. More precisely, we see here significant slowdown of the leading edge of the x-ray pulse. In other words, the group velocity v_g of the leading edge of the pulse becomes smaller than c. The explanation of this can be found in Fig. 2, which shows clearly the transfer of the front of the pulse backward in the course of propagation. This demonstrates the strong deviation of the refractive index from $n_0 \approx 1$ because of the nonlinearity,

$$n = n_0 + n_{\rm nl} \approx 1 + n_{\rm nl}. \tag{18}$$

In fact, the strong compression of the pulse (Fig. 6) is also a manifestation of this light-induced change of the refractive index. We compute the velocity of the pulse as the speed of propagation of its leading edge,

$$v_g = \frac{dy}{dt} \approx \frac{y_n - y_{n-1}}{t_{\max}(y_n) - t_{\max}(y_{n-1})}. \tag{19}$$

Here $t_{\max}(y_n)$ is the instant when the pulse at $y = y_n$ takes maximum. We call this speed the group velocity of the leading edge of the XFEL pulse. What strikes the eye is the strong decrease of the group velocity (up to 78% from the speed of the light c in vacuum). Such a slowdown of the pulse being not surprising in the optical region is very unusual in the x-ray dispersion where the deviation of the refractive index n from 1 in equilibrium conditions is smaller than 10^{-4}. We point out that the nonlinearity results in a change of the index of refraction $n_0 \to n_0 + n_{\rm nl}$ with an effective nonlinear refractive index of the order $n_{\rm nl} \sim 0.1$–1. The effect of the slowdown of the strong XFEL pulse resembles the deceleration of the solitons [15].

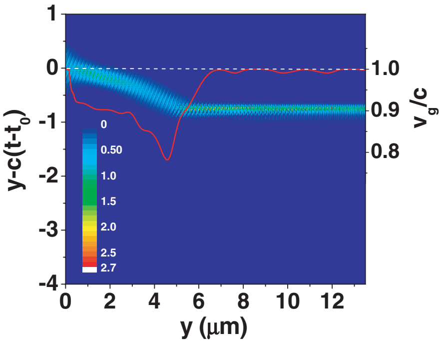

FIG. 13. (Color online) Trajectory of the total pulse $I(t, y) = |E(t, y)H(t, y)|$ (10^{18} W/cm^2) in the local frame and the group velocity v_g (red solid line). Linear geometry. Gaussian input pulse: $\theta = 3\pi$, $\tau = 2$ fs. The pulse trajectory in the vacuum is shown by the dashed line.

The dependence of the group velocity $v_g(N, y)$ and pulse compression on the concentration N deserves a special comment. The temporal reshaping of the pulse and its compression do not depend on the concentration in the sense that the decrease of the concentration from N to N' results in the same temporal shape of the pulse, only at a longer propagation distance $y' = yN/N'$ [see discussion of Eqs. (9) and (10)]. The picture is different for the group velocity (19) which changes as

$$\frac{c}{v_g(N', y')} - 1 = \frac{N'}{N}\left[\frac{c}{v_g(N, y)} - 1\right]. \tag{20}$$

C. Focusing geometry

The simulations for linear geometry presented earlier in this article show that mainly the front of the pulse is compressed. This compression is limited, because the area of the front of the pulse decreases during propagation. To compensate for this decrease of the pulse area, one can use the focusing of the light, which can make the compression stronger [17,31]. To describe the pulse propagation with the focusing, we need to solve the 2D Maxwell equations, which is rather time consuming. Instead, we follow the model of Gibbs and Slusher [17] of the incoming uniform spherical wave (see Sec. II).

1. $\tau = 2\,fs$ and $\tau = 4\,fs$

The propagation of the input Gaussian pulses with $\tau = 2$ fs and $\tau = 4$ fs is shown in Fig. 14. Due to the focusing, the peak intensity grows during propagation. The comparison of Fig. 6(B) and Fig. 14(A) demonstrates that the focusing does not improve the compression for $\tau = 2$ fs. However, Fig. 14 shows that the focusing makes the compression of

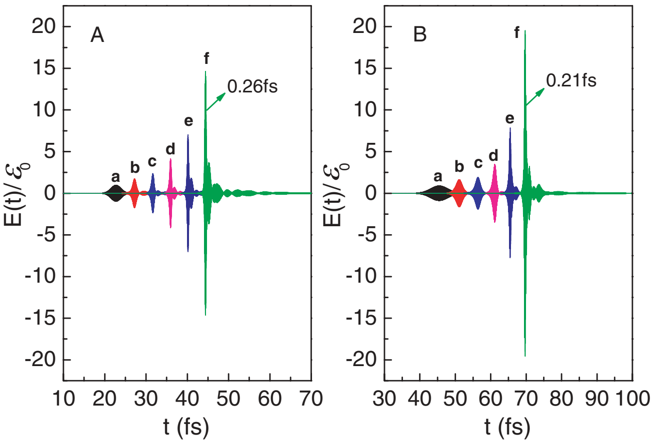

FIG. 14. (Color online) Focusing geometry. Gaussian 3π input pulse. The temporal shapes of the pulse for different propagation lengths $\Delta r = 0$, 1.27, 2.54, 3.81, 5.08, 6.35 and μm are marked by the labels a, b, c, d, e, and f, respectively. $R = 7.35$ μm. (A) $\tau = 2$ fs, $\mathcal{E}_0 = 2.91 \times 10^9$ V/cm, $I_0 = 1.12 \times 10^{16}$ W/cm^2, the photon flux $s_0 = 2.85 \times 10^{32}$ photon/(cm^{2}s). (B) $\tau = 4$ fs, $\mathcal{E}_0 = 1.45 \times 10^9$ V/cm, $I_0 = 2.81 \times 10^{15}$ W/cm^2, the photon flux $s_0 = 7.15 \times 10^{31}$ photon/(cm^{2}s).

the 4-fs pulse orders of magnitude stronger than that seen with linear geometry (0.21 fs instead of 2.2 fs with the linear geometry). The formation of the spectrum is now different because the inversions are seen along the whole propagation length (6.35 μm) for both pulses. The spectrum for the 2-fs input pulse is formed mainly by the frequencies near the pump transition ω_{10} [Fig. 15(A)]. The Stokes component near ω_{12} is much weaker in the studied region $\Delta r \leqslant 6.35$ μm. In contrast, the 4-fs input pulse generates a rather strong Stokes SRRS band [Fig. 15(B)].

2. *$\tau = 6$ fs and $\tau = 10$ fs*

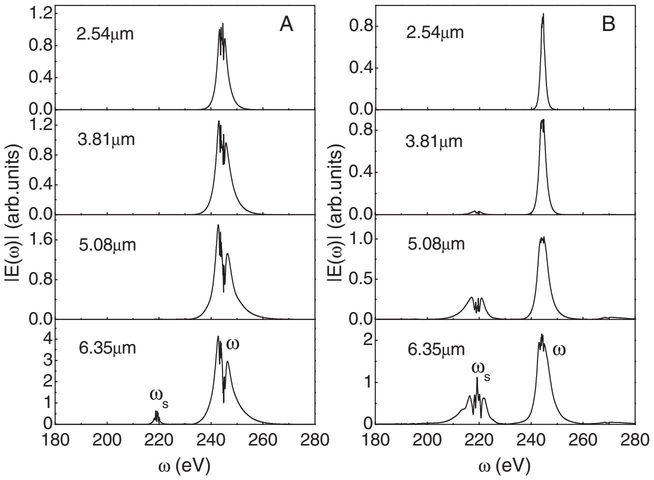

FIG. 15. Focusing geometry. Gaussian 3π input pulse. The spectrum $|E(\omega)|$ for different propagation lengths $\Delta r = 2.54$, 3.81, 5.08, and 6.35 μm. $R = 7.35$ μm. The parameters are the same as in Fig. 14. (A) $\tau = 2$ fs. (B) $\tau = 4$ fs.

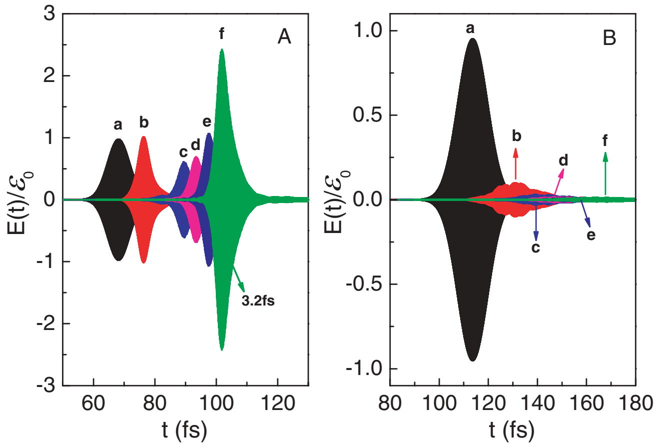

FIG. 16. (Color online) Focusing geometry. Gaussian 3π input pulse. The temporal shapes of the pulse for different propagation lengths $\Delta r = 0$, 1.27, 2.54, 3.81, 5.08, and 6.35 μm are marked by the labels a, b, c, d, e, and f, respectively. $R = 7.35$ μm. (A) $\tau = 6$ fs, $\mathcal{E}_0 = 9.69 \times 10^8$ V/cm, $I_0 = 1.25 \times 10^{15}$ W/cm^2, the photon flux $s_0 = 3.19 \times 10^{31}$ photon/(cm^{2}s). (B) $\tau = 10$ fs, $\mathcal{E}_0 = 5.81 \times 10^8$ V/cm, $I_0 = 4.48 \times 10^{14}$ W/cm^2, the photon flux $s_0 = 1.15 \times 10^{31}$ photon/(cm^{2}s).

We compute the dynamics of the input Gaussian pulse for the pulse durations ($\tau = 6$ fs and 10 fs) which are longer than the lifetime of the core-excited state $1/\Gamma = 5.5$ fs. A twofold compression (up to 3.2 fs) is seen only for the 6-fs pulse (Fig. 16). This pulse also generates a strong Stokes band [Fig. 17(A)] and weak four-wave mixing sidebands. The Stokes band generated by the 10-fs pulse is much weaker: $|E(\omega_{12})/E(\omega_{10})| \approx 0.02$ at $y = 6.35$ μm [Fig. 17(B)].

D. Role of the direct ionization

The simulations shown in the previous sections were performed without taking into account the channel of direct ionization of the $3s$ and $3p$ electrons, $\gamma^{(k)}(t) = 0$. One should

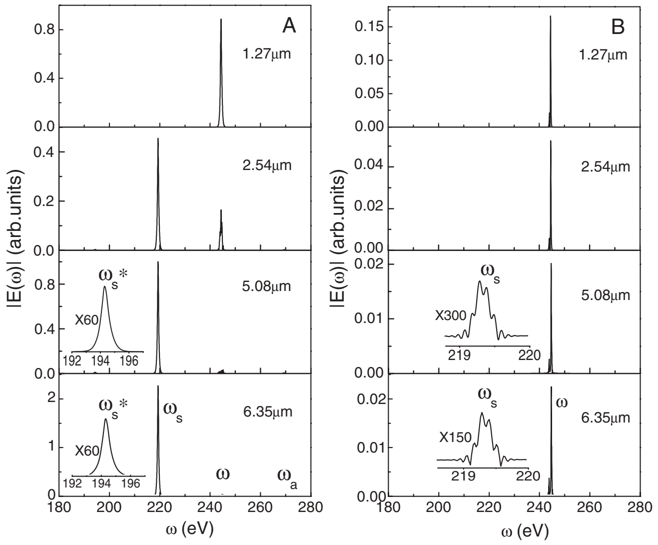

FIG. 17. Focusing geometry. Gaussian 3π input pulse. The spectrum $|E(\omega)|$ for different propagation lengths $\Delta r = 1.27$, 2.54, 5.08, and 6.35 μm. $R = 7.35$ μm. The parameters are the same as in Fig. 16 (A) $\tau = 6$ fs. (B) $\tau = 10$ fs.

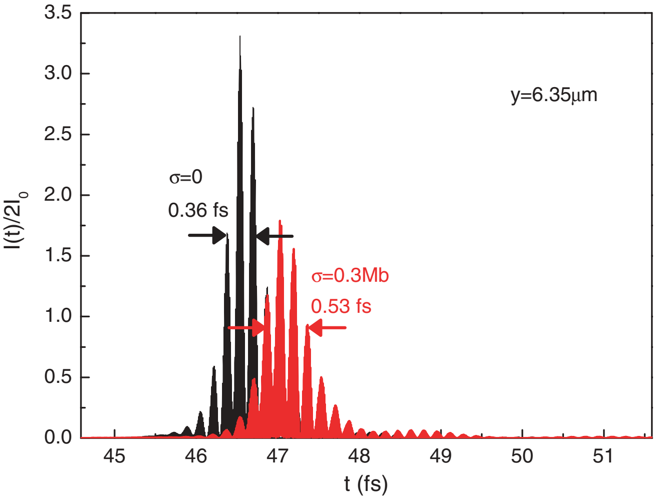

FIG. 18. (Color online) Linear geometry. Gaussian 3π input pulse. $\tau = 2$ fs, $I_0 = 1.12 \times 10^{16}$ W/cm^2. Intensity distribution of the pulse at $y = 6.35$ μm in the medium without [$\sigma = 0$, black (dark) line] and with [$\sigma = 0.3$ Mb, red (light gray) line] direct photoionization. The origin of the fine structure [$\Delta t = 0.17$ fs; see Eq. (13)] is the beating between the pump and Stokes fields.

keep in mind that the direct ionization of the $2p$ electrons is absent in our case because ω is below the ionization threshold of the $2p_{3/2}$ level. Let us now include in calculations the channel of direct ionization. We compute the rate of direct ionization $\gamma^{(k)}(t)$ (6) using the experimental ionization cross section [24] $\sigma \approx 0.3$ Mb. It is a reasonable approximation to use the same value of the photoionization cross sections for the ground, core-excited, and final states $\sigma \approx \sigma_0 \approx \sigma_1 \approx \sigma_2$, because the main ionization channel is the ionization of the $3p$ electrons. Figure 18 shows that the only role of the direct photoionization is the slight decrease of the compression of the pulse (0.53 fs instead of 0.36 fs). The development of the Stokes field and of the four-wave mixing components are almost the same as in the case where the direct ionization is neglected (Fig. 19). The main reason for this is the rather long photoionization time $\tau_{\text{ph}} = 1/\gamma_{\text{ph}}^{\max} \approx 11.7$ fs in comparison with the pulse duration $\tau = 2$ fs.

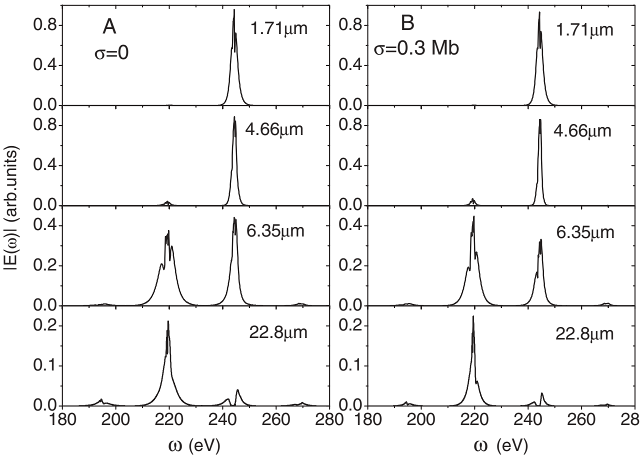

FIG. 19. The spectrum of the XFEL pulse at different propagation distances. (A) The direct ionization is neglected ($\sigma = 0$). (B) The direct photoionization is taken into account ($\sigma = 0.3$ Mb). The other parameters are the same as in Fig. 18.

Our model neglects the interaction of the light with ionized atoms that have shifted resonant energies. This approximation is valid for propagation distances studied here because the number of ionized atoms is smaller than 10% for the intensity $\approx 10^{16}$ W/cm^2 being used here. Indeed, the amount of the core-excited ions (<10%) created by the resonant absorption $2p_{3/2} \rightarrow 4s$ followed by ionization of the valence electrons $(3s, 3p)$ is much smaller than the number of the core-excited intact atoms. This means that the gain coefficient for core-excited ions is smaller by one order of magnitude. Due to this, the possible stimulated emission from the ions will have a rather high intensity for longer propagation distances (about one order of magnitude larger than the length of formation of the SRRS for the neutral Ar atoms).

It is worth mentioning that the role of ionization decreases for longer pulses with the same pulse area $\mathcal{E}\tau \approx$ const. The first impression is that the decrease of the peak value of the ionization rate $\gamma^{(k)}(t) \propto \mathcal{E}^2$ is compensated by the longer duration τ. However, this compensation is not complete because the total probability of the ionization $P_{\text{ion}} \propto \mathcal{E}^2\tau \propto 1/\tau$ decreases as $1/\tau$. The numerical simulations confirm this simple estimation.

V. SUMMARY

We study the propagation through the resonant medium of the intense x-ray pulses from an XFEL. The XFEL pulse experiences during propagation strong temporal and spectral reshaping because of the stimulated resonant Raman scattering which starts from the ASE and is followed later on by the LWI. To exemplify the theory, simulations are performed for x-ray pulses with the carrier frequency tuned in resonance with the $2p_{3/2}$-$4s$ transition in Ar. Simulations show strong deformation of the pulse during propagation. One can see the extensive ringing structure delayed relative to the pump pulse. The spectrum of the pulse changes during propagation. First of all, one can see the fine spectral structure near the pump transition caused by the dynamical Stark effect. Then the Stokes spectral band arises. The scenario of the lasing near the Stokes frequency is as follows: The temporal reshaping of the pulse results in a broadening of the initial spectral distribution as well as the formation of the weak extensive tail. Such a deformation of the initially narrow spectral distribution gives enough light near the Stokes and four-wave mixing lines to trigger the SRRS process. The interference of the Stokes and pump waves results in a beating which eliminates the inversion. The quenching of the inversion is followed by the LWI which strongly amplifies the Stokes field because the competitive ASE channel at the pump frequency is expelled. Simulations show also the compression of the x-ray pulse (up to 0.1 fs) during propagation, which is stronger for the focusing geometry of the pulse propagation. The compression effect is seen for the pulse duration shorter or comparable with the lifetime of the core-excited state. The pump x-ray pulse generates a strong Stokes component, as well as two weaker anti-Stokes and Stokes sidebands induced by four-wave mixing. The pulse reshaping in resonant medium results in a slowdown of the XFEL pulse which moves with a group velocity up to 78% of the speed of light in vacuum. This means an anomalously large (for x-ray region) change of the refractive index (about 22%) due to the nonlinearity. The deceleration of the pulse by resonant medium can be used as the x-ray delay line.

ACKNOWLEDGMENTS

We acknowledge support from the Swedish Research Council (VR), Carl Tryggers Stiftelse (CTS) foundation and Grant No. 2006CB806000 of National Basic Research Program for China.

---

[1] L. H. Yu *et al.*, Science **289**, 932 (2000).
[2] C. Bressler and M. Chergui, Chem. Rev. **104**, 1781 (2004).
[3] T. Tschentcher, Chem. Phys. **299**, 271 (2004).
[4] http://xfel.desy.de/science/sti_meeting_2004/.
[5] E. L. Saldin, E. A. Schneidmiller, and M. V. Yurkov, Phys. Rev. ST Accel. Beams **9**, 050702 (2006).
[6] I. V. Schweigert and S. Mukamel, Phys. Rev. A **78**, 052509 (2008).
[7] D. M. Healion, I. V. Schweigert, and S. Mukamel, J. Phys. Chem. A **112**, 11449 (2008).
[8] M. Meyer *et al.*, Phys. Rev. A **74**, 011401(R) (2006).
[9] J. Schulz *et al.*, Phys. Rev. A **74**, 012705 (2006).
[10] J.-C. Liu, Y. Velkov, Z. Rinkevicius, H. Ågren, and F. Gel'mukhanov, Phys. Rev. A **77**, 043405 (2008).
[11] M. O. Scully and M. S. Zubairy, *Quantum Optics* (Cambridge University Press, Cambridge, UK, 2001).
[12] F. Gel'mukhanov and H. Ågren, Phys. Rev. A **49**, 4378 (1994).
[13] F. Gel'mukhanov and H. Ågren, Phys. Rep. **312**, 87 (1999).
[14] A. L. Cavalieri *et al.*, Nature (London) **449**, 1029 (2007).
[15] A. Yariv, *Quantum Electronics* (John Wiley & Sons, New York, 1975).
[16] V. Kimberg, S. Polyutov, F. Gel'mukhanov, H. Ågren, A. Baev, Q. Zheng, and G. S. He, Phys. Rev. A **74**, 033814 (2006).
[17] H. M. Gibbs and R. E. Slusher, Appl. Phys. Lett. **18**, 505 (1971).
[18] B. Lengerer, C. G. Schroer, M. Kuhlmann, B. Benner, T. F. Günzler, O. Kurapova, F. Zontone, A. Snigirev, and I. Snigireva, J. Phys. D: Appl. Phys. **38**, A218 (2005).
[19] J.-C. Liu, C.-K. Wang, and F. Gel'mukhanov, Phys. Rev. A **76**, 053804 (2007).
[20] A. Nilsson, O. Björneholm, B. Hernnäs, A. Sandell, and N. Mårtensson, Surf. Sci. **293**, L835 (1993).
[21] K. Siegbahn, C. Nordling, G. Johansson, J. Hedman, P. F. Heden, K. Hamrin, U. Gelius, T. Bergmark, L. O. Werme, and Y. Baer, *ESCA Applied to Free Molecules* (North-Holland, Amsterdam-London, 1969).
[22] D. A. Shaw, G. C. King, F. H. Read, and D. Cvejanovic, J. Phys. B **15**, 1785 (1982).
[23] S. L. Sorensen, T. Åberg, J. Tulkki, E. Rachlew-Källne, G. Sundström, and M. Kirm, Phys. Rev. A **50**, 1218 (1994).
[24] R. Haensel, G. Keitel, N. Kosuch, U. Nielsen, and P. Schreiber, J. Phys. Paris **32**, C4-236 (1971).
[25] M. Nakamura *et al.*, Phys. Rev. Lett. **21**, 1303 (1968).
[26] Dalton, References in http://www.kjemi.uio.no/software/dalton/
[27] J. Feldhaus, E. L. Saldin, J. R. Schneider, E. A. Schneidmiller, and M. V. Yurkov, Opt. Commun. **140**, 341 (1997).
[28] E. L. Saldin, E. A. Schneidmiller, and M. V. Yurkov, Nucl. Instrum. Methods A **445**, 178 (2000).
[29] E. L. Saldin, E. A. Schneidmiller, Yu. V. Shvyd'ko, and M. V. Yurkov, Nucl. Instrum. Methods A **475**, 357 (2001).
[30] D. C. Burnham and R. Y. Chiao, Phys. Rev. **188**, 667 (1969).
[31] S. L. McCall and E. L. Hahn, Phys. Rev. **183**, 457 (1969).
[32] W. Miklaszewski and J. Fiutak, Z. Phys. B **93**, 491 (1994).
[33] B. J. Herman, J. H. Eberly, and M. G. Raymer, Phys. Rev. A **39**, 3447 (1989).
[34] B. Ya. Zel'dovich, N. F. Pilipetsky, and V. V. Shkunov, *Principles of Phase Conjugation* (Springer-Verlag, Berlin, 1985), Springer Series in Optical Sciences, Vol. 42.